

pubs.acs.org/crystal Article

Insights into the Polymorphic Structures and Enantiotropic Layer-Slip Transition in Paracetamol Form III from Enhanced Molecular Dynamics

Richard S. Hong, Eric J. Chan, Leslie Vogt-Maranto, Alessandra Mattei, Ahmad Y. Sheikh, and Mark E. Tuckerman*



Cite This: Cryst. Growth Des. 2021, 21, 886-896



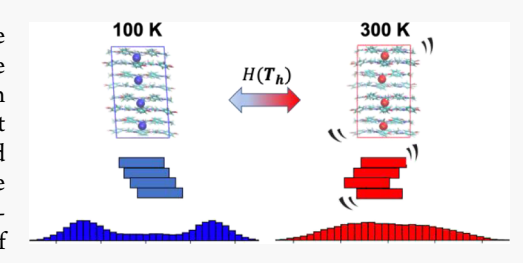
ACCESS

Metrics & More

Article Recommendations

Supporting Information

ABSTRACT: Reversible temperature-mediated solid phase changes, otherwise known as enantiotropic transformations, occur in many molecular crystals. These transformations take place as a result of the free-energy stabilization through entropic contributions at finite temperatures and can often have significant implications for the properties of crystalline solids. As such, understanding and predicting these transformations is of great importance. In this study, we utilize molecular simulations to elucidate the mechanism behind the enantiotropic layer-slip phase transformation between the orthorhombic and monoclinic versions of paracetamol form III (form III-m and III-o). Using standard molecular dynamics



(MD) in addition to crystal adiabatic free-energy dynamics, an MD-based enhanced sampling approach for crystalline systems, we demonstrate that the transformation from the monoclinic form III-m to the orthorhombic form III-o is driven by localized and dynamic disorder within the structure rather than a perfect crystal-to-crystal transition. These results suggest that the orthorhombic form III-o structure does not exist as a perfect orthorhombic crystal with fully aligned layers, but rather, as an entropy-stabilized collective ensemble average of various misaligned layer-slipped structures. Overall, these simulation approaches, which explicitly treat dynamic structural disorder, allowed us to map out the free-energy landscape of this enantiotropic transformation as a function of temperature and extract critical insights into the underlying mechanism of the transformation.

■ INTRODUCTION

Many organic molecular crystals can exist in multiple distinct polymorphs, which are known to have different physical and chemical properties, a fact that has significant implications in areas ranging from pharmaceuticals to explosives, organic semiconductors, and agrochemicals. Since extensive experimental screening and characterization of polymorphs are often highly resource-intensive and can lead to significant gaps in the overall understanding of a full crystal form landscape and relationships therein, significant efforts have been made to develop computational methodologies to predict accessible and energetically stable polymorphs starting from the simple 2-D molecular chemical diagram.

In the last 20 years, significant progress has been achieved in the field of computational crystal structure prediction (CSP), as demonstrated by the results from the most recent blind test of organic crystal structure methods organized by the Cambridge Crystallographic Data Center (CCDC).⁷ A standard CSP approach randomly generates many single-crystal structures from a global search, quickly ranks their stabilities according to lattice energies from a force field (FF), and refines their relative lattice energies using dispersion-corrected density functional theory (DFT) calculations.⁹ Although this approach generates an energy ranking of each predicted polymorph, it is only able to capture the relative stability of the predicted

structures at 0 K and is now generally referred to as "CSP_0". 12 As such, the standard CSP does not describe reversible, temperature-mediated polymorphic transitions, otherwise known as enantiotropic transformations. Nyman et al. have shown that more than 20% of the polymorphic pairs in a dataset of more than 500 compounds likely exhibit enantiotropic transformations.¹³ These temperature-mediated phase transitions can have significant implications on the control, performance, and characteristics of crystalline solids. 14 The timescale for enantiotropic transitions can vary, with many occurring too slowly to be of experimental importance or so quickly that the crystal rapidly converts to another structure under experimental conditions. However, some compounds exhibit solid-phase enantiotropic transformations on timescales that are relevant during processing and formulation steps.¹⁴ For instance, solid-phase enantiotropic transformations can occur under cold storage or high-temperature drying or

Received: September 9, 2020 Revised: December 21, 2020 Published: January 5, 2021





processing of pharmaceuticals, as demonstrated by the polymorphic transition of artemisinin during hot melt extrusion. Hence, a mechanistic understanding and prediction of these transformations is of great importance. 19

Enantiotropic transformations are conventionally thought to occur either as continuous-phase transformations, in which the respective polymorphic pairs exist as co-existing phases²⁰ or as immediate martensitic-like phase transformations, where concerted-like displacements occur between neighboring molecular pairs. 14,21 The martensitic transformation is a type of discontinuous first-order displacive transition, whereas continuous-phase transitions are often denoted as secondorder and subdivided into either displacive or order-disorder regimes.^{22,23} All the different models consider enantiotropic transformations as a phase transition from one crystal polymorph to another, for which the free-energy differences can be estimated from the difference between the two endpoint structures. As such, various methods have been developed to capture entropic and finite-temperature contributions to the crystal-structure relative free energy. These methods include the use of the quasi-harmonic approximation or the Einstein Crystal method, where an anharmonic crystalline supercell is driven to its harmonically restrained state and then finally connected to its ideal Einstein Crystal state through thermodynamic integration. 24-29 However, since these methods model crystalline systems as perfect repeating crystals, they may either fail to capture anharmonic low frequency modes of motion (in the case of the harmonic and quasi-harmonic approximations) or stabilizing effects of dynamic disorder often occurring at ambient temperatures. 13 Such contributions of anharmonic motions and static or dynamic disorder to temperature-mediated phase transformations have been demonstrated experimentally by singlecrystal diffuse scattering studies on polymorphs of benzocaine^{30,31} and have been explored computationally as well.^{32,33} In addition, these methods cannot capture actual transformations between different structures.

Molecular dynamics (MD) can, in theory (and practice), be used to understand the energetics and mechanisms of enantiotropic transformations. MD is a computational approach for generating the motion of every atom in a physical system as a function of time by numerically solving Newton's equations of motion for each atom in the system. Typically, the forces exerted on each particle are described by empirically parameterized FFs that capture various types of molecular interactions such as molecular bond bending and stretching, Coulombic interactions, and intermolecular van der Waals interactions.³⁴ However, because of the inherently high energy barriers associated with crystalline polymorphic transitions and the timescale associated with these transitions compared to a currently feasible MD simulation, standard MD approaches often fail to capture accurately the behavior and thermodynamics of crystalline-phase transformations.

As such, enhanced sampling techniques, such as crystal adiabatic free-energy dynamics (Crystal-AFED),³⁵ can be used to generate a statistically significant number of energetic barrier-crossing events associated with the structural transformations, allowing the corresponding free energies to be extracted. Briefly, Crystal-AFED targets a set of pre-selected collective variables, capable of distinguishing different crystalline states, for sampling enhancement via a carefully orchestrated combination of high temperature and adiabatic decoupling (see Methods section below for details). The

application of Crystal-AFED and its subsequent enhancements³⁵ has been demonstrated in capturing and understanding the free-energy landscape of various polymorphs of benzene and naphthalene, ^{36,37} elucidating the melting mechanisms of copper and aluminum, ³⁸ generating solid—solid phase transformations in solid molybdenum³⁹ (which employed a related approach), ^{40,41} studying polymorphs of one of the targets in the recent sixth CCDC blind structure prediction test, ⁷ and testing the stability of high-entropy polymorphs of benzamide. ⁴²

In this study, we use standard MD and Crystal-AFED simulations to study the enantiotropic transformation between the layered orthorhombic and monoclinic versions of paracetamol form III, termed forms III-0 and III-m, as reported by Reiss et al.⁴³ Although paracetamol form I is used in the commercial pharmaceutical formulations, metastable polymorphs such as forms II and III potentially allow for improvements in both the solubility and dissolution rate, hence, improving the overall bioavailability. In addition, the compressibility of form I is poor, rendering tableting difficult. Paracetamol forms II and III, being more compressible, would be preferable for pharmaceutical formulations; however, these forms have generally been more difficult to crystallize. 44,45

It has been suggested that paracetamol III may garner more attention soon because of possible "open-air up-scalable" growth of this form. However, a precise description of the form III-m and, particularly, the form III-o remains elusive (with similar difficulties surrounding form II^{46}). The enantiotropic transition between the low-temperature stable form III-m and the high-temperature stable form III-o is reported to occur between 170 and 220 K, with the orthorhombic form III-o structure breaking symmetry into a higher Z' structure at lower temperatures (Figure 1). ⁴³ The

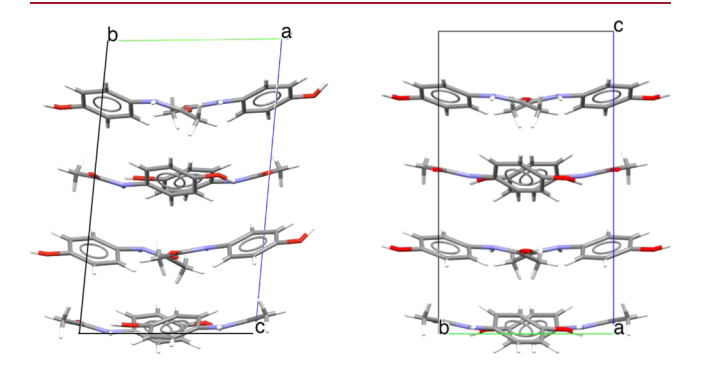


Figure 1. CCDC-deposited crystal structure of (left) the monoclinic (space group Pc11) form III-m with an α angle of 84.16° and (right) the orthorhombic (space group $Pca2_1$) form III-o with an α angle of 90° .

predominant distinguishing feature between these two polymorphs is the unit cell α angle where the monoclinic form (in the non-standard setting) and orthorhombic form exhibit α angles of 84.16° and 90°, respectively.

Although the transition occurs at very low temperatures, the findings from this study provide important insights into the behavior of crystalline solids at experimental or process-relevant temperatures. We intend to show from this study, using the III-o and III-m pair as an example, an enantiotropic transformation that occurs as a result of dynamic disorder rather than as a phase transformation from one perfect static crystal to another. We demonstrate that the appearance of

independent localized motions in the structure at higher temperatures results in local domains of disorder, which manifest as different thermally averaged structures that have also been observed experimentally by powder X-ray diffraction (PXRD). In addition to probing the mechanism of the transition, we are able to use our methods to map out the free-energy landscape of this phase transition. We aim to show from this study the sometimes-complex mechanisms by which dynamic disorder can stabilize crystal structures at finite temperatures, even as low as 200 K. Although the paracetamol III-o and III-m pair was used as an example for this study, this phenomenon may likely occur in many other enantiotropically related polymorphic pairs.

METHODS

FF and Initial Structure. The GAFF (Generalized Amber Force Field) and the set of AM1-BCC charges were used for this system, as assigned by the antechamber program. The GAFF has proven to be successful in predicting the crystal morphology, crystal structures, and polymorphism under electric fields for paracetamol. Crystal structures of paracetamol III-o (HXACAN-40) and III-m (HXACAN-39) were obtained from the Cambridge Structural Database (CSD) and are based on CSP results (III-o) or matching PXRD data (III-m). The crystal structures were optimized and were compared to the initial deposited CSD structures using the Crystal Packing Similarity Tool available in Mercury 3.10.3. Relative lattice energies were determined using the runprep program in the UPACK package. The optimized structures were used to create 2 × 2 × 2 supercells containing 64 molecules. All MD simulations reported in the main text were performed starting with a supercell of the optimized III-o form, with comparison to simulations starting from III-m reported in the Supporting Information.

Molecular Dynamics. MD simulations were performed using the PINY_MD package so with the GAFF inter- and intramolecular potentials. The initial supercells from UPACK were minimized in PINY_MD using 2000 steps of steepest descent minimization. The minimized structures were then equilibrated for 25 ps with constant volume isothermal (*NVT*) MD runs at the specified temperatures. Temperature control in the *NVT* MD simulations was achieved using massive Nosé-Hoover chain (NHC) thermostats so, seek (length = 4, τ = 20 fs, Suzuki-Yoshida order = 7, multiple time step = 4) with 0.5 fs for each time step. After *NVT* equilibration, flexible-cell isothermalisobaric (NPTF) MD simulations were run at the specified temperatures and pressures, using the atomic positions and velocities from the preceding *NVT* simulations as the initial condition. NPTF MD simulations were run using the Martyna–Tobias–Klein barostat and an NHC thermostat on the barostat with τ = 100 fs. see section of the section of the

Crystal Adiabatic Free-Energy Dynamics. We used Crystal-AFED in order to generate a statistically significant number of energetic barrier-crossing events associated with the structural transformations, allowing the corresponding free energies to be extracted. The Crystal-AFED method and its variants originate from the ${\rm AFED}^{61}$ method and its driven analog 40 where the system is adiabatically decoupled from a set of chosen collective variables (CVs), or a set of associated coarse-grained variables, that are maintained at a temperature much higher than the system being studied. The CVs are chosen for their ability to distinguish different relevant configurational basins on the energy landscape. The high temperature assigned to the collective variable allows energy barriers in the simulation to be crossed efficiently, while a large mass is assigned to the collective variables of interest in order to ensure adiabatic decoupling from the system being studied. Adiabatic decoupling is required for accurate extraction of the free-energy profiles from this method.

The equations of motion of Crystal-AFED, similar in form to those of Martyna, Tobias, and Klein, 59 generate an anisotropic isobaric isothermal (NPT) ensemble. Here, the components of the simulation box, or the cell matrix (\mathbf{h} matrix), are used as collective variables. Each

element of the cell matrix is coupled to a generalized Gaussian moment thermostat 62 which is maintained at the specified high fictitious cell temperature $T_{\rm h}$, where $T_{\rm h}\gg T$, where T is the physical temperature studied. A large effective mass was assigned to the barostat to ensure adiabatic decoupling of the cell matrix to the system. More details of the Crystal-AFED method, including the equations of motion, are described in the Supporting Information.

DFT Optimization. DFT optimizations of the crystal structures were performed using the Gaussian/plane wave (GPW)⁶³ scheme in CP2K.^{64,65} Both structures were optimized using the PBE exchange—correlation functional⁶⁶ with the D3(BJ) dispersion correction⁶⁷ and TZVP-MOLOPT-GTH basis set and the corresponding GTH pseudopotentials were used with an energy cutoff of 900 Ry.^{68,69}

Trajectory Histogram and Free-Energy Calculations. Histograms of the cell lattice α angle visited throughout the simulation trajectory were created using 40 bins. Folded histograms were created as well by subtracting any angle greater than 90° from 180°. For example, a cell α angle of 95° was counted in the histogram as 85°. The resulting histograms and free-energy profiles were determined up to 90° and were symmetrized about 90°. The purpose was to provide a more extended view of the free-energy profile that clearly shows how the transformation occurs on either side of α = 90°. The free energies from the simulations were calculated using the Boltzmann distribution, as shown in eq 1

$$\Delta G_i = -k_b \hat{T} \ln p_i \tag{1}$$

where $k_{\rm b}$ is the Boltzmann constant, \hat{T} represents either the molecular temperature of the simulation for NPTF MD simulations or the fictitious cell temperature for Crystal-AFED simulations, 36 p_i represents the probability in bin i of the histogram that the α angle is visited throughout the trajectory, and ΔG_i is the free energy in bin i. The calculated free energies were normalized by the total number of molecules per layer pair, which represents the total number of molecules per layer-slip interface. The units are labeled "kJ/mol per layer pair".

■ RESULTS AND DISCUSSION

DFT and FF Minimization. Both FF and DFT minimizations were first performed on the structures to obtain an understanding of the static energy values of these two deposited CCDC structures. The FF-minimized III-o and IIIm structures matched well with CCDC-deposited structures with an RMSD₁₅ of 0.307 Å and 0.296 Å, respectively. The FF optimization preserved the distinctive differences in the α angles, which are 82.33° and 90°, respectively, for the optimized III-m and III-o structures. The FF energies predict form III-m to be the more stable structure by 0.96 kJ/mol while DFT minimization energies predict form III-m to be more stable by 0.53 kJ/mol. The DFT-optimized structures of III-o and III-m matched well with the CCDC-deposited structures with an RMSD₁₅ of 0.178 Å for both structures. The RMSD₁₅ between the two DFT-optimized structures is 0.28 Å, with α angles of 83.85 and 90° for the III-m and III-o forms, respectively. The energies from FF and DFT minimizations were consistent with experimental finding that form III-m is the stable form at lower temperatures. In addition, the similarity in the energy differences between the FF and DFT minimizations, as well as the similarity between the FFminimized structure and the CCDC-deposited crystal structure confirms the ability of this set of FF parameters to describe the system being studied. However, although our DFT and FF optimizations are consistent with experimental findings, these static calculations are not able to describe the energetics, dynamics, and behavior of the crystals at realistic, finite temperatures and pressures.

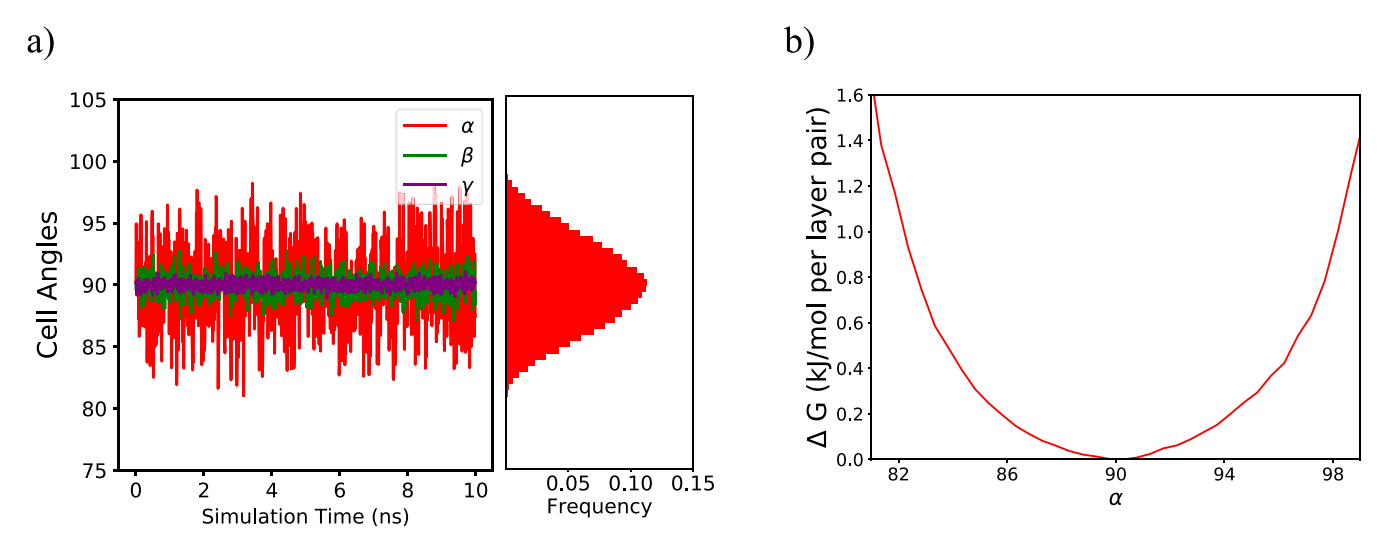


Figure 2. (a) Supercell α , β , and γ angles over an NPTF MD trajectory and the corresponding histogram of the α angle at 300 K. (b) Free-energy difference as a function of the α angle.

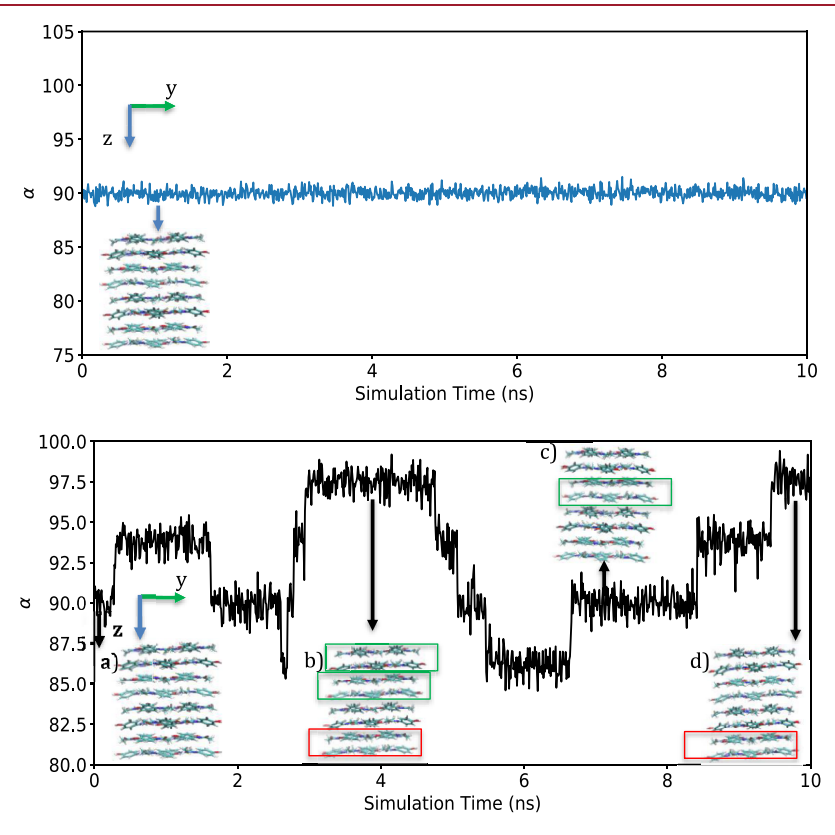


Figure 3. Supercell α angles throughout a 10 ns NPTF run at 50 K (top) and 100 K (bottom), starting with the form-III-o structure. Snapshots throughout the trajectory of the 100 K simulation show the existence of various layer-slipstates. The red boxes highlight layer slippage in the negative y direction while the green boxes highlight layer slippage in the positive y direction. Structure snapshots were viewed along the x axis or the crystallographic a axis.

MD Simulations at Room Temperature. The results of the isothermal-isobaric (NPTF) MD simulations were examined on both the FF-optimized supercells of the monoclinic and orthorhombic forms to probe the behavior of the structures at 300 K. The temperature of 300 K was chosen to correspond to the single-crystal structure of form III-0 proposed using the indexed PXRD unit cell parameters at 300 K.⁴⁵ Over the course of 10 ns NPTF runs at 300 K on the form III-0 structure, we observe constant changes and fluctuations in the cell α angle (Figure 2), a parameter capable

of distinguishing between form III-0 and form III-m. Throughout the simulation, the crystal supercell interconverts between monoclinic and orthorhombic states as shown by the α angle fluctuations. At this temperature, the sampling is sufficiently rapid to converge the α angle distribution in just 10 ns. For the simulation to be fully converged, the simulation cell must visit each of these different relevant α angle states many times throughout the simulation. Figure 2 shows the free-energy profile as a function of the α angle extracted from the trajectory. The prediction of a more stable orthorhombic phase

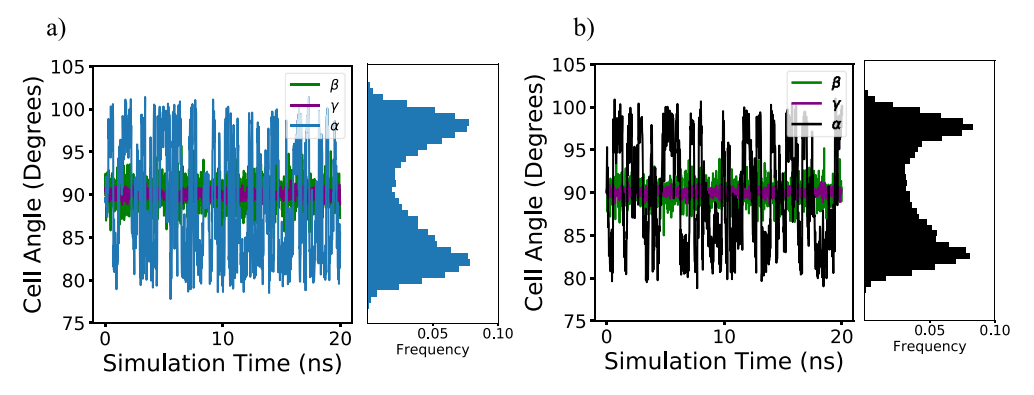


Figure 4. Supercell throughout a Crystal-AFED trajectory and its corresponding histograms at (a) 50 K with $T_h = 750$ K and (b) 100 K with $T_h = 500$ K.

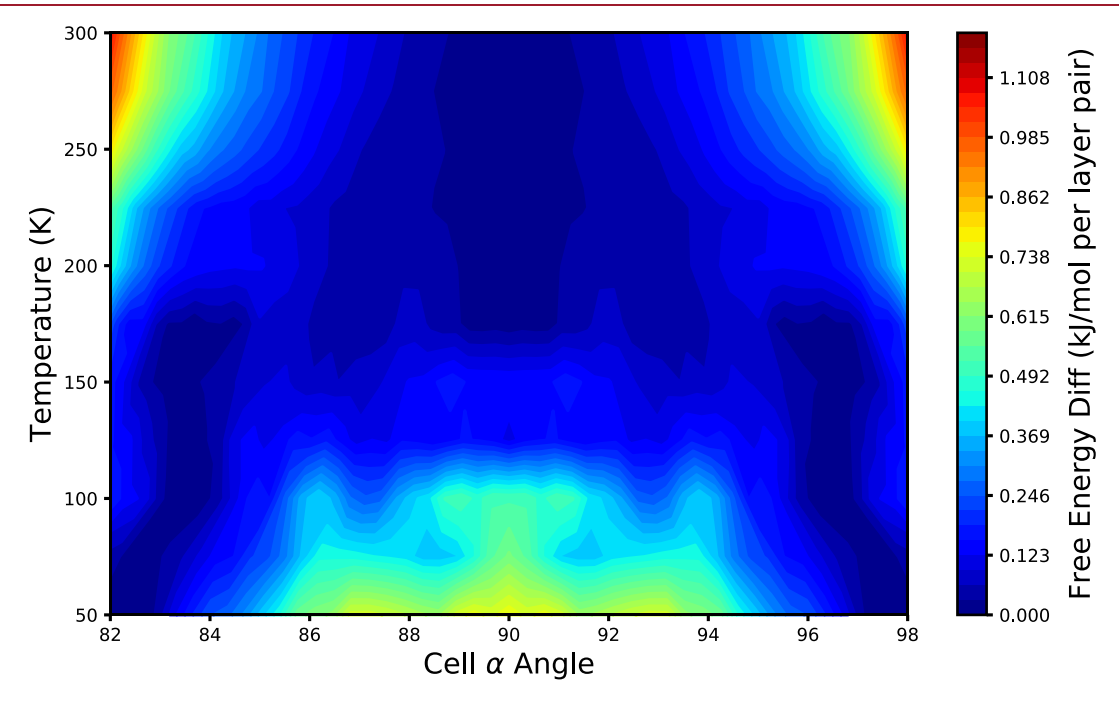


Figure 5. 2D contour plot of the free-energy surface as a function of temperature and cell α angle.

from the free-energy profile is in agreement with the published experimental observations by Reiss, et al., ⁴³ according to which the orthorhombic structure is the solid form observed at room temperature.

MD Simulations at Lower Temperatures. The nature of the structural transition changes at temperatures well below room temperature. To this end, simulations were performed at 50 and 100 K in order to probe this behavior. Unfortunately, as shown in Figure 3, standard NPTF simulations at these temperatures produce no transitions at 50 K and only rare transitions at 100 K over 10 ns. The reason for this is the presence of a substantial energy barrier that cannot be easily crossed at these temperatures. At 100 K, the trajectory of the α shows several metastable states corresponding to layer slipping (see Figure 3). Because of the difficulty of generating proper structural transitions at such low temperatures, enhanced sampling techniques must be employed. Therefore, we ran Crystal-AFED simulations at fictitious cell temperatures of $T_{\rm h}$ = 500 K and 750 K, depending on the physical temperature, with an effective barostat mass large enough to ensure adiabaticity. The use of Crystal-AFED in this study is analogous to finding a high enough fictitious cell temperature

to gently nudge the system over energetic barriers. A large enough effective mass on the barostat is also required to allow the motions of the molecules to relax and react to this gentle push before the system is "nudged" again.

From a 20 ns Crystal-AFED run at physical temperatures of 50 and 100 K, we observe that the simulation is able to escape its minima and readily sample and explore other states as a function of α (Figure 4). Similar to the NPTF simulations, the changes in the supercell angle are a result of localized layer slips within the supercell. Compared to the standard NPTF runs at these lower temperatures, the Crystal-AFED runs allow the simulation cell to visit the different energetic basins repeatedly over a relatively short run, resulting in an efficient convergence of the free-energy profile.

From Crystal-AFED simulations at lower temperatures (from 50 to 150 K), a histogram was created for the different α angles visited throughout the trajectory. The free-energy profile was then determined using eq 1 using the fictitious cell temperature of Crystal-AFED as \hat{T} . By combining the Crystal-AFED simulations at lower temperatures (from 50 to 150 K) and standard NPTF runs at higher temperatures (from 175 to 300 K), we were able to obtain the free-energy profile of the

phase transformation as a function of both temperature and α angle (Figure 5). To build this profile, simulations were performed at 25 K intervals between 50 and 300 K with 40 different contour levels used to represent the free-energy differences. The values of the points between the simulated temperatures were determined through linear interpolation on a triangular mesh. To confirm that Crystal-AFED generates a similar free-energy profile as a converged standard NPTF MD, both simulations were performed at 150 and 175 K, and the resulting free-energy profiles are shown in the Supporting Information. Since the histograms of the simulations are close to symmetric, the histograms were folded across 90°, and symmetrized for the purpose of presentation. The full freeenergy histograms at each temperature are shown in the Supporting Information. The resulting free-energy curves for different supercell sizes are also shown in the Supporting Information.

The free-energy plot shows that the minimum shifts from a monoclinic structure at lower temperatures from 50 to 100 K with an α angle ranging from 82 to 84°, to an orthorhombic structure at higher temperatures above 200 K, where the free-energy minimum with respect to α angle lies at 90°. The transition from the simulations occurs around 175 K, as shown by the coexistence of the energy minima at the monoclinic and orthorhombic α angles. These results are in agreement with the published experimental observations where the transition is reported to occur between 170 and 220 K.

Monoclinic-to-Orthorhombic Transformation. In order to elucidate the mechanism of the monoclinicorthorhombic transformation of paracetamol, the layer-slip behavior at various temperatures was studied. The aim was to probe whether this transformation from the monoclinic to the orthorhombic structure occurs in a highly concerted manner from one perfectly aligned crystal to another, or if the orthorhombic structure results from an ensemble average of different misaligned layers. One method to do so is by calculating the "layer-slip measure", $\delta_{\rm LS}$, an order parameter introduced to quantify the layer misalignment of the structures throughout the simulation. In order to calculate the value of δ_{LS} , the differences in the y-positions in the centers of mass of each pair of layers were first determined. Differences between these calculated values were then determined for each neighboring layer pair and their absolute values were added together, as shown in eq 2

$$\begin{split} \delta_{LS} &= |(Y_3 - Y_2) - (Y_2 - Y_1)| + |(Y_4 - Y_3) - (Y_3 - Y_2)| + \\ |(Y_2 - Y_1) - (Y_4 - Y_3)| + |(Y_4 - Y_1') - (Y_4 - Y_3)| + \\ |(Y_4 - Y_1') - (Y_3 - Y_2)| + |(Y_4 - Y_1') - (Y_2 - Y_1)| + \\ |(Y_4 - Y_2) - (Y_3 - Y_1)| \end{split}$$

where Y_1 refers to the center of mass of layer pair 1, Y_2 refers to the center of mass of layer pair 2, Y_3 refers to the center of mass of layer pair 3, Y_4 refers to the center of mass of layer pair 4, and Y_1' refers to the center of mass of the periodic image of layer pair 1. A value of the layer-slip measure close to zero represents perfectly aligned layers, as observed in the CCDC-deposited III-m or III-o structure, and larger values represent larger extents of layer misalignment. The layer-slip measure was used as an order parameter in this case rather than the mean-squared displacement since the mean-squared displacement uses the trajectory-averaged centers of mass and cannot

quantify layer alignment in a monoclinic structure. Further details on how these values were determined are explained in the Supporting Information.

By determining the layer slippage throughout the MD trajectories at varying temperatures, we observe that the lower-temperature simulations exhibit a smaller degree of layer slip than the higher-temperature simulations (Figure 6), suggesting

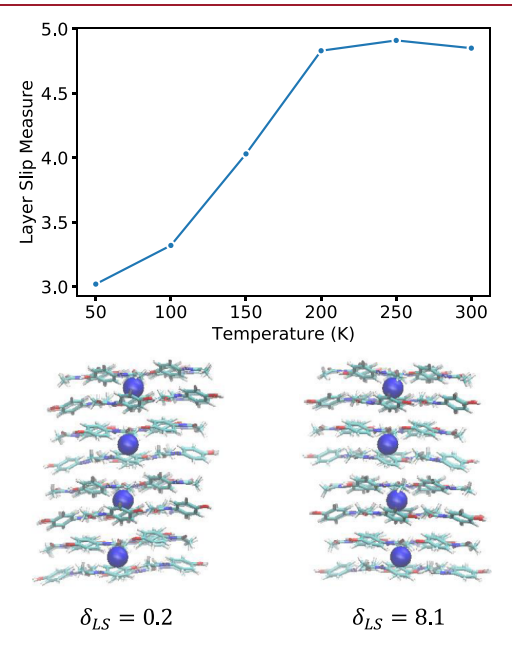


Figure 6. (top) Simulation trajectory-average layer-slip measure as a function of temperature. (bottom) Example structures from the simulation trajectory with varying levels of layer misalignment. The left structure exhibits a very low layer-slip measure and is representative of a perfectly aligned cell, while the right structure exhibits a very high layer-slip measure, representative of a layer-misaligned structure.

a larger degree of layer-slip disorder and misalignment at higher temperatures. In addition, this relationship shows that the locations of layers in the III-o structure are generally independent of their respective neighbors.

Although the calculations of the layer-slip measure can quantify the overall average magnitude of layer misalignment in the simulations, they do not describe how correlated the layer-slip motions are in the simulation. In order to probe this correlation, we determined the displacement correlation coefficients of the layer slips along the y direction for each neighboring layer pair at different temperatures using the following steps:

- the centers of mass of each layer pair in the simulation supercell and the trajectory-averaged center of mass for each layer pair were determined;
- 2) the *y*-displacement of the center of mass for each layer pair with respect to the trajectory average was determined at each time point; and
- 3) the correlation coefficient between layer slips of neighboring pairs was calculated to discover if the layer slips are correlated. The correlation coefficients were determined as a Pearson correlation coefficient, which determines the strength of the linear association between two variables.

From the calculated displacement correlation coefficients between neighboring pairs in the supercell, we observe a decrease in the displacement correlation with increasing temperature, suggesting that the layers in the higher-temperature simulations move more independently of their respective neighbors as temperature increases (Figure 7). The correlation

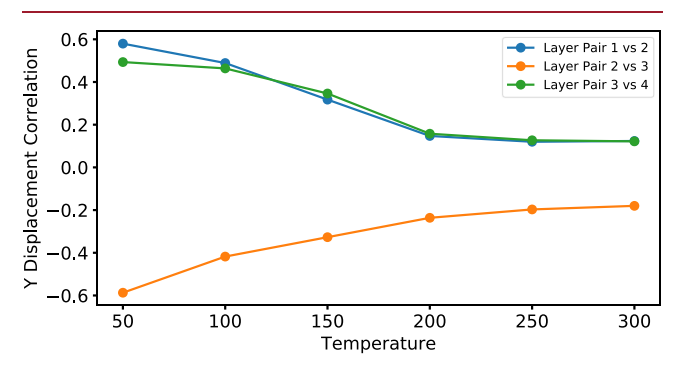


Figure 7. Trajectory-average layer-slip correlation coefficients of each neighboring layer pair in the supercell vs temperature.

coefficients between non-neighboring layer pairs were determined as well for larger supercells at 100 K and 300 K and the results are shown in the Supporting Information. The decrease in layer-slip correlations at 300 K suggests that there

are likely more possible combinations of layer-pair positions that can contribute to an averaged orthorhombic structure.

In order to confirm this hypothesis, we constructed a histogram of the *y*-displacements for each layer pair over the trajectory in order to probe the distribution of layer-slip movements in the simulation (Figure 8). In addition, structural snapshots were taken from the simulation trajectory to show examples of how different structures are related to various points on each of the histograms. These histograms were determined, again, with respect to the trajectory-averaged center of mass for each layer pair, where the origin is placed at the center of the simulation cell.

From the histograms of the y-displacements generated over the course of the simulation trajectory, we observe that the 100 K simulation exhibits a bimodal shape with distinct displacements, while the 300 K simulation exhibits a broad yet unimodal distribution. The broadened distribution at 300 K suggests that there are likely more combinations of layer-slip displacements and positions that average out to a putative orthorhombic structure. This is confirmed through the structural snapshot from the simulation trajectory, where we observe that the orthorhombic structure can be made of many possible different combinations of layer-pair arrangements rather than a perfectly aligned supercell.

Paracetamol Form III Intermolecular Bonding. In order to gain an understanding of how certain structural

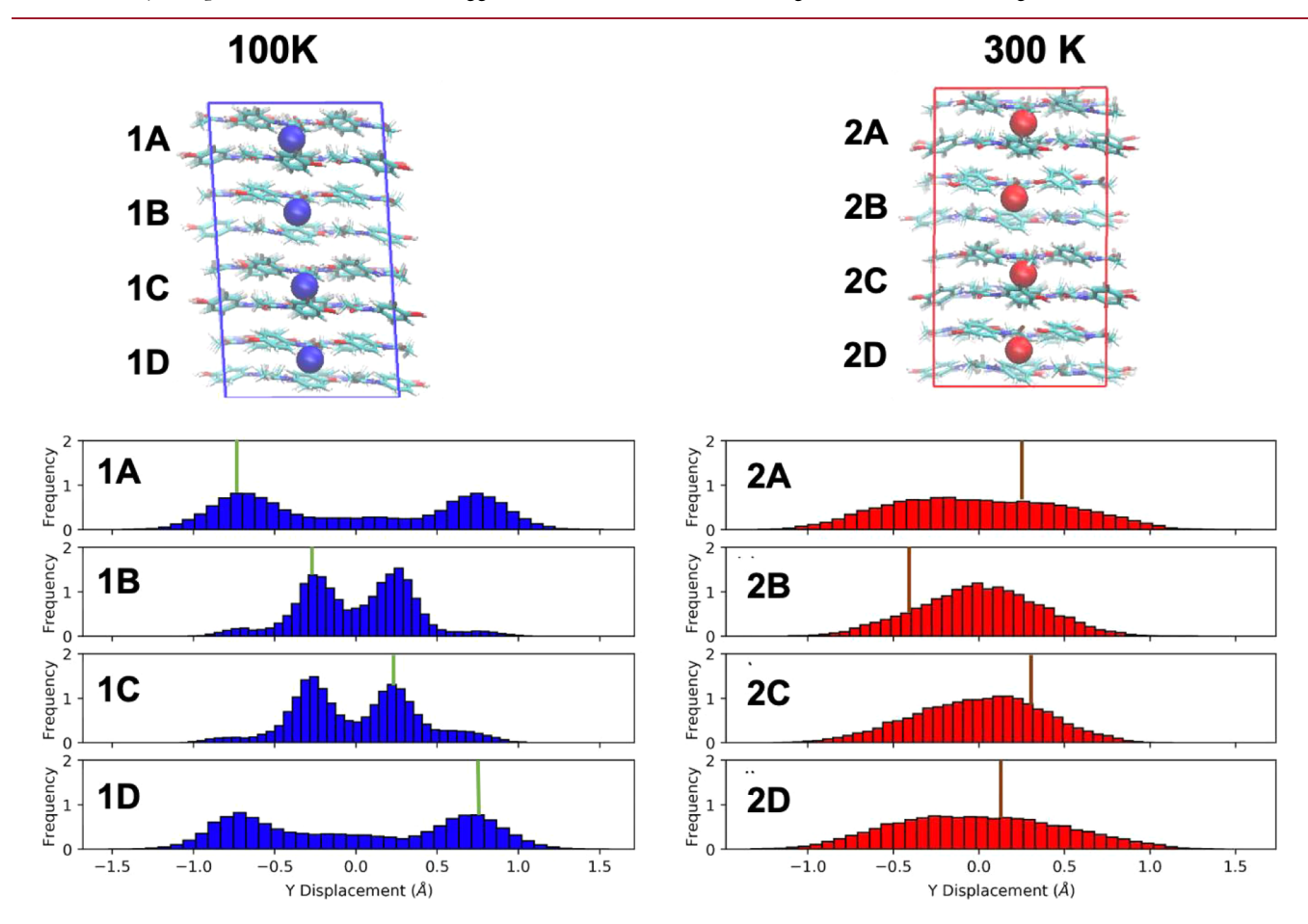
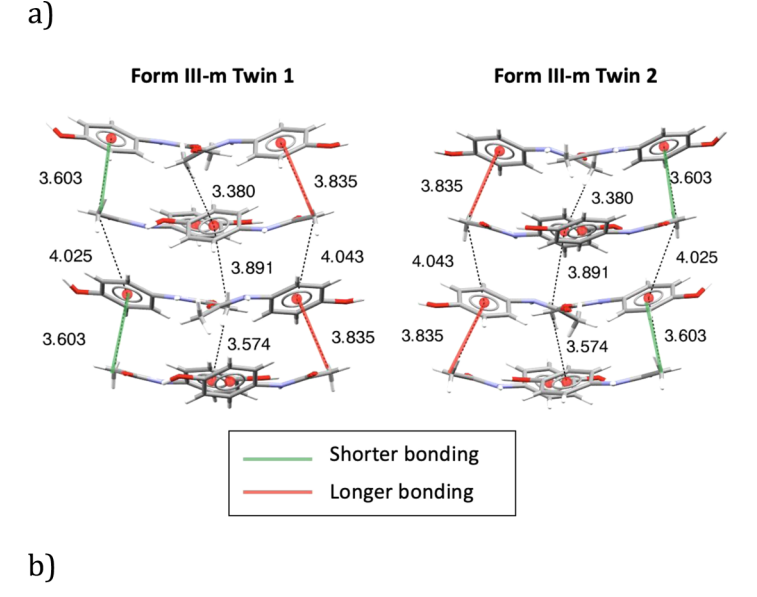


Figure 8. Histogram of layer center of mass displacements with respect to the trajectory average for 100 and 300 K for (a) layer pair 1, (b) layer pair 2, (c) layer pair 3, and (d) layer pair 4. The green lines on the histogram mark the displacements of each layer pair for structure 1, a perfect monoclinic supercell at 100 K, while the brown lines on the 300 K histogram mark the displacements of each layer pair for structure 2, a misaligned orthorhombic supercell. The coordinate origin for these simulations is placed at the center of the unit cell.



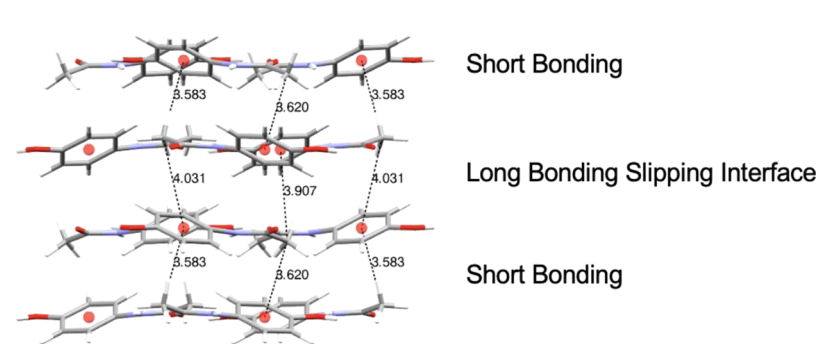


Figure 9. (a) Structural analysis of two twins of the form III-m structure showing interchanging short- and long-bonding interactions (comparing intra-layer pair). (b) Structural analysis of the form III-o crystal structure showing shorter methyl—phenyl bond lengths for non-slipping layer interfaces and longer-bonding distances for slipping layer interfaces (comparing inter-layer pair).

motifs may result in these types of dynamic behaviors, the intermolecular bonding arrangements of the crystal structures of form III-m and form III-o were analyzed. One such interaction that stands out is the weak methyl-phenyl interaction between each layer pair in both the monoclinic and orthorhombic structures (Figure 9). Upon inspection of the monoclinic structures, there exists alternating short and long methyl-phenyl interactions within each individual layer pair. Between the two monoclinic form III twin structures that are observed predominantly throughout the low-temperature simulations with α angles of 82 and 98°, respectively, we observe interchanged methyl-phenyl interaction distances, leading us to hypothesize that the layer movements and transitions between monoclinic twins, especially in the lowtemperature simulations, are driven by the competing interactions between these intra-layer pair short and long methyl-phenyl interactions throughout the entire structure. The observation of a bimodal distribution of displacements in the low-temperature simulations suggests that competition between the intra-layer short and long interactions result in a double-well potential of mean force separating the two monoclinic twins.

In addition, we observe from the simulation that uncorrelated layer slippage occurs as layer pairs rather than individual layer slips, where layer slippage occurs through specific interfaces in the crystal structure. The analysis of the crystal structure shows that the "slipping" interfaces exhibit shorter methyl—phenyl interactions (Figure 9). This suggests that within the double-layered form III structure, the long-bonding slipping interface is more prone to disorder and layer slips, while the short-bonding interfaces generally displace together in a correlated manner.

In order to understand how these methyl—phenyl bond distances in the "slipping" layer interfaces change between the monoclinic and orthorhombic structures, a pair distribution function was calculated between the interacting methyl and phenyl centers of mass at each of the layer-slipping interfaces (Figure 10). The pair distribution functions at 50 K and 100 K computed from the Crystal-AFED simulations show more distinct peaks corresponding to more ordered intermolecular interactions within the structure, while the 300 K simulation exhibits a broadened distribution. Like the observed layer-pair displacement histograms, these pair distribution functions show that the 300 K orthorhombic structure exists as an ensemble average of disordered structures possessing varying intermolecular bond distances.

CONCLUSIONS

Paracetamol form III is an important crystalline phase because of its potential pharmaceutical use, yet its structural features have remained elusive. Our study has investigated the enantiotropic transformation of paracetamol form III-m to

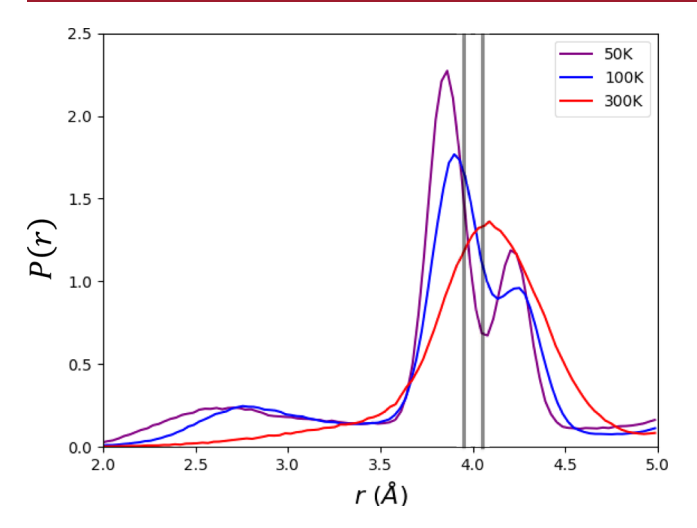


Figure 10. Pair distribution function of interaction of methyl and phenyl centroids for the molecules on the layer-slipping interfaces. The gray lines represent the bonding distances corresponding to a perfect form III-o structure.

form III-o. The results from standard MD and Crystal-AFED simulations demonstrate that the mechanism of this enantiotropic transformation is related to local disorder due to dynamic layer-slip displacements. Thus, form III-o is an orthorhombic supercell built from a thermal ensemble average of layer-slipped structures rather than a perfectly aligned orthorhombic structure. In addition, consistent with experimental observations, we showed using standard NPTF and Crystal-AFED that the free-energy minimum of form III as a function of the crystallographic cell angle α shifts from a monoclinic cell toward an orthorhombic cell with increasing temperature. Overall, this study demonstrates the complexity underlying how dynamic disorder can stabilize crystal structures at finite temperatures, which may not be captured with the current state-of-the-art methodologies in CSP. Although this study primarily focused on the effect of layerslip disorder on the enantiotropic transformation of paracetamol form III, we believe that this type of phenomenon can occur for many other enantiotropic polymorphic pairs and can be thoroughly studied using MD and enhanced sampling.

■ ASSOCIATED CONTENT

Supporting Information

The Supporting Information is available free of charge at https://pubs.acs.org/doi/10.1021/acs.cgd.0c01250.

Equations of motion of Crystal-AFED; comparisons of free-energy curves from Crystal-AFED and NPTF simulations; full histograms of angles throughout the simulation trajectories; comparisons of free-energy curves with larger supercells; scatter plot of neighboring layer-pair displacements at 100 and 300 K; displacement scatter plots for non-neighboring layer pairs at 100 and 300 K; description of the calculation of the layer-slip measure; and simulation free-energy comparisons between the use of III-o and III-m as an initial structure (PDF)

AUTHOR INFORMATION

Corresponding Author

Mark E. Tuckerman — Department of Chemistry, New York University, New York City, New York 10003, United States; Courant Institute of Mathematical Sciences, New York University, New York 10012, United States; NYU-ECNU Center for Computational Chemistry at NYU Shanghai, Shanghai 200062, China; orcid.org/0000-0003-2194-9955; Email: Mark.Tuckerman@nyu.edu

Authors

Richard S. Hong — Department of Chemistry, New York University, New York City, New York 10003, United States; Process Research and Development, AbbVie Inc, North Chicago, Illinois, United States; orcid.org/0000-0002-4214-6847

Eric J. Chan — Department of Chemistry, New York
University, New York City, New York 10003, United States
Leslie Vogt-Maranto — Department of Chemistry, New York
University, New York City, New York 10003, United States;
orcid.org/0000-0002-7006-4582

Alessandra Mattei — Process Research and Development, AbbVie Inc, North Chicago, Illinois, United States Ahmad Y. Sheikh — Process Research and Development, AbbVie Inc, North Chicago, Illinois, United States; orcid.org/0000-0002-5972-3938

Complete contact information is available at: https://pubs.acs.org/10.1021/acs.cgd.0c01250

Notes

The authors declare no competing financial interest.

ACKNOWLEDGMENTS

This work was primarily supported by the New York University Materials Research Science and Engineering Center (MRSEC) program of the National Science Foundation under award number DMR-1420073. M.E.T. additionally acknowledges support from the National Science Foundation award no. CHE-1955381. Abbvie partially funded the study, contributed to the design, participated in the collection, analysis, interpretation of the data, and writing, reviewing, and approval of the final publication. R.H., A.M., and A.Y.S. are employees of AbbVie and may own AbbVie stock.

REFERENCES

- (1) Caira, M. R. Crystalline Polymorphism of Organic Compounds. In *Design of Organic Solids*; Weber, E., Aoyama, Y., Caira, M. R., Desiraju, G. R., Glusker, J. P., Hamilton, A. D., Meléndez, R. E., Nangia, A., Eds.; Springer: Berlin, Heidelberg, 1998; pp 163–208.
- (2) Li, T.; Mattei, A. Pharmaceutical Crystals: Science and Engineering; Wiley, 2018.
- (3) Yang, Z.; Zeng, Q.; Zhou, X.; Zhang, Q.; Nie, F.; Huang, H.; Li, H. Cocrystal explosive hydrate of a powerful explosive, HNIW, with enhanced safety. *RSC Adv.* **2014**, *4*, 65121–65126.
- (4) Bae, Y. J.; Kang, G.; Malliakas, C. D.; Nelson, J. N.; Zhou, J.; Young, R. M.; Wu, Y.-L.; Van Duyne, R. P.; Schatz, G. C.; Wasielewski, M. R. Singlet Fission in 9,10-Bis(phenylethynyl)-anthracene Thin Films. J. Am. Chem. Soc. 2018, 140, 15140–15144.
- (5) Yang, J.; Hu, C. T.; Zhu, X.; Zhu, Q.; Ward, M. D.; Kahr, B. DDT Polymorphism and the Lethality of Crystal Forms. *Angew. Chem.* **2017**, *56*, 10165–10169.
- (6) Zhu, X.; Hu, C. T.; Yang, J.; Joyce, L. A.; Qiu, M.; Ward, M. D.; Kahr, B. Manipulating Solid Forms of Contact Insecticides for

Infectious Disease Prevention. J. Am. Chem. Soc. 2019, 141, 16858–16864.

- (7) Reilly, A. M.; Cooper, R. I.; Adjiman, C. S.; Bhattacharya, S.; Boese, A. D.; Brandenburg, J. G.; Bygrave, P. J.; Bylsma, R.; Campbell, J. E.; Car, R.; Case, D. H.; Chadha, R.; Cole, J. C.; Cosburn, K.; Cuppen, H. M.; Curtis, F.; Day, G. M.; DiStasio Jr, R. A.; Dzyabchenko, A.; van Eijck, B. P.; Elking, D. M.; van den Ende, J. A.; Facelli, J. C.; Ferraro, M. B.; Fusti-Molnar, L.; Gatsiou, C.-A.; Gee, T. S.; de Gelder, R.; Ghiringhelli, L. M.; Goto, H.; Grimme, S.; Guo, R.; Hofmann, D. W. M.; Hoja, J.; Hylton, R. K.; Iuzzolino, L.; Jankiewicz, W.; de Jong, D. T.; Kendrick, J.; de Klerk, N. J. J.; Ko, H.-Y.; Kuleshova, L. N.; Li, X.; Lohani, S.; Leusen, F. J. J.; Lund, A. M.; Lv, J.; Ma, Y.; Marom, N.; Masunov, A. E.; McCabe, P.; McMahon, D. P.; Meekes, H.; Metz, M. P.; Misquitta, A. J.; Mohamed, S.; Monserrat, B.; Needs, R. J.; Neumann, M. A.; Nyman, J.; Obata, S.; Oberhofer, H.; Oganov, A. R.; Orendt, A. M.; Pagola, G. I.; Pantelides, C. C.; Pickard, C. J.; Podeszwa, R.; Price, L. S.; Price, S. L.; Pulido, A.; Read, M. G.; Reuter, K.; Schneider, E.; Schober, C.; Shields, G. P.; Singh, P.; Sugden, I. J.; Szalewicz, K.; Taylor, C. R.; Tkatchenko, A.; Tuckerman, M. E.; Vacarro, F.; Vasileiadis, M.; Vazquez-Mayagoitia, A.; Vogt, L.; Wang, Y.; Watson, R. E.; de Wijs, G. A.; Yang, J.; Zhu, Q.; Groom, C. R. Report on the sixth blind test of organic crystal structure prediction methods. Acta Crystallogr., Sect. B: Struct. Sci. 2016, 72, 439-459.
- (8) Price, S. L.; Braun, D. E.; Reutzel-Edens, S. M. Can computed crystal energy landscapes help understand pharmaceutical solids? *Chem. Commun.* **2016**, *52*, 7065–7077.
- (9) Zhang, P.; Wood, G. P. F.; Ma, J.; Yang, M.; Liu, Y.; Sun, G.; Jiang, Y. A.; Hancock, B. C.; Wen, S. Harnessing Cloud Architecture for Crystal Structure Prediction Calculations. *Cryst. Growth Des.* **2018**, *18*, *6891–6900*.
- (10) Neumann, M. A. Tailor-Made Force Fields for Crystal-Structure Prediction. J. Phys. Chem. B 2008, 112, 9810-9829.
- (11) Woodley, S. M.; Catlow, R. Crystal structure prediction from first principles. *Nat. Mater.* **2008**, *7*, 937–946.
- (12) Price, S. L. Is zeroth order crystal structure prediction (CSP_0) coming to maturity? What should we aim for in an ideal crystal structure prediction code? *Faraday Discuss.* **2018**, *211*, 9–30.
- (13) Nyman, J.; Day, G. M. Modelling temperature-dependent properties of polymorphic organic molecular crystals. *Phys. Chem. Chem. Phys.* **2016**, *18*, 31132–31143.
- (14) Kawakami, K. Reversibility of Enantiotropically Related Polymorphic Transformations from a Practical Viewpoint: Thermal Analysis of Kinetically Reversible/Irreversible Polymorphic Transformations. J. Pharm. Sci. 2007, 96, 982–989.
- (15) Bauer, J. F. Drying Pharmaceutical Solids-Hydrates and Enantiotropic Polymorphs. J. Validation Technol. 2009, 15, 49-56.
- (16) Alsirawan, M. B.; Paradkar, A. Impact of the Polymorphic Form of Drugs/NCEs on Preformulation and Formulation Development. In *Innovative Dosage Forms: Design and Development at Early Stage*; Bachhav, Y., Ed.; Wiley, 2019; pp 1–47.
- (17) Kulkarni, C.; Kendrick, J.; Kelly, A.; Gough, T.; Dash, R. C.; Paradkar, A. Polymorphic transformation of artemisinin by high temperature extrusion. *CrystEngComm* **2013**, *15*, 6297–6300.
- (18) Horosanskaia, E.; Seidel-Morgenstern, A.; Lorenz, H. Investigation of drug polymorphism: Case of artemisinin. *Thermochim. Acta* **2014**, *578*, 74–81.
- (19) Gui, Y.; Yao, X.; Guzei, I. A.; Aristov, M. M.; Yu, J.; Yu, L. A Mechanism for Reversible Solid-State Transitions Involving Nitro Torsion. *Chem. Mater.* **2020**, 32, 7754–7765.
- (20) Ruggiero, M. T.; Axel Zeitler, J.; Korter, T. M. Concomitant polymorphism and the martensitic-like transformation of an organic crystal. *Phys. Chem. Chem. Phys.* **2017**, *19*, 28502–28506.
- (21) Gunn, E.; Guzei, I. A.; Cai, T.; Yu, L. Polymorphism of Nifedipine: Crystal Structure and Reversible Transition of the Metastable β Polymorph. Cryst. Growth Des. **2012**, 12, 2037–2043.
- (22) Dove, M. T. Theory of displacive phase transitions in minerals. *Am. Mineral.* **1997**, *82*, 213–244.

- (23) Dove, M. T. Introduction to Lattice Dynamics; Cambridge University Press: Cambridge, 1993.
- (24) Carlos Vega, E. G. N. Revisiting the Frenkel-Ladd method to compute the free energy of solids: The Einstein molecule approach. *J. Chem. Phys.* **2007**, *127*, 154113.
- (25) Dybeck, E. C.; Abraham, N. S.; Schieber, N. P.; Shirts, M. R. Capturing Entropic Contributions to Temperature-Mediated Polymorphic Transformations Through Molecular Modeling. *Cryst. Growth Des.* **2017**, *17*, 1775–1787.
- (26) Frenkel, D.; Ladd, A. J. C. New Monte Carlo method to compute the free energy of arbitrary solids. Application to the fcc and hcp phases of hard spheres. *J. Chem. Phys.* **1984**, *81*, 3188–3193.
- (27) Kapil, V.; Engel, E.; Rossi, M.; Ceriotti, M. Assessment of Approximate Methods for Anharmonic Free Energies. *J. Chem. Theory Comput.* **2019**, *15*, 5845–5857.
- (28) Dybeck, E. C.; Schieber, N. P.; Shirts, M. R. Effects of a More Accurate Polarizable Hamiltonian on Polymorph Free Energies Computed Efficiently by Reweighting Point-Charge Potentials. *J. Chem. Theory Comput.* **2016**, *12*, 3491–3505.
- (29) Yang, M.; Dybeck, E.; Sun, G.; Peng, C.; Samas, B.; Burger, V. M.; Zeng, Q.; Jin, Y.; Bellucci, M. A.; Liu, Y.; Zhang, P.; Ma, J.; Jiang, Y. A.; Hancock, B. C.; Wen, S.; Wood, G. P. F. Prediction of the Relative Free Energies of Drug Polymorphs above Zero Kelvin. *Cryst. Growth Des.* **2020**, 20, 5211–5224.
- (30) Chan, E. J.; Welberry, T. R.; Goossens, D. J.; Heerdegen, A. P.; Beasley, A. G.; Chupas, P. J. Single-crystal diffuse scattering studies on polymorphs of molecular crystals. I. The room-temperature polymorphs of the drug benzocaine. *Acta Crystallogr., Sect. B: Struct. Sci.* **2009**, *65*, 382–392.
- (31) Chan, E. J.; Welberry, T. R. Precursor effects of the orthorhombic to monoclinic phase transition in benzocaine form (II) revealed by X-ray diffuse scattering. *Acta Crystallogr., Sect. B: Struct. Sci.* **2010**, *66*, 260–270.
- (32) Dybeck, E. C.; McMahon, D. P.; Day, G. M.; Shirts, M. R. Exploring the Multi-minima Behavior of Small Molecule Crystal Polymorphs at Finite Temperature. *Cryst. Growth Des.* **2019**, *19*, 5568–5580.
- (33) Shtukenberg, A. G.; Zhu, Q.; Carter, D. J.; Vogt, L.; Hoja, J.; Schneider, E.; Song, H.; Pokroy, B.; Polishchuk, I.; Tkatchenko, A.; Oganov, A. R.; Rohl, A. L.; Tuckerman, M. E.; Kahr, B. Powder diffraction and crystal structure prediction identify four new coumarin polymorphs. *Chem. Sci.* **2017**, *8*, 4926–4940.
- (34) Gelpí, J. L.; Hospital, A.; Goñi, J. R.; Orozco, M. Molecular dynamics simulations: advances and applications. *Adv. Appl. Bioinf. Chem.* **2015**, *8*, 37–47.
- (35) Yu, T.-Q.; Chen, P.-Y.; Chen, M.; Samanta, A.; Vanden-Eijnden, E.; Tuckerman, M. Order-parameter-aided temperature-accelerated sampling for the exploration of crystal polymorphism and solid-liquid phase transitions. *J. Chem. Phys.* **2014**, *140*, 214109.
- (36) Yu, T.-Q.; Tuckerman, M. E. Temperature-Accelerated Method for Exploring Polymorphism in Molecular Crystals Based on Free Energy. *Phys. Rev. Lett.* **2011**, *107*, 015701.
- (37) Schneider, E.; Vogt, L.; Tuckerman, M. E. Exploring polymorphism of benzene and naphthalene with free energy based enhanced molecular dynamics. *Acta Crystallogr., Sect. B: Struct. Sci.* **2016**, 72, 542–550.
- (38) Samanta, A.; Tuckerman, M. E.; Yu, T.-Q.; E, W. Microscopic mechanisms of equilibrium melting of a solid. *Science* **2014**, *346*, 729.
- (39) Rogal, J.; Schneider, E.; Tuckerman, M. E. Neural-Network-Based Path Collective Variables for Enhanced Sampling of Phase Transformations. *Phys. Rev. Lett.* **2019**, *123*, 245701.
- (40) Abrams, J. B.; Tuckerman, M. E. Efficient and Direct Generation of Multidimensional Free Energy Surfaces via Adiabatic Dynamics without Coordinate Transformations. *J. Phys. Chem. B* **2008**, *112*, 15742–15757.
- (41) Cuendet, M. A.; Margul, D. T.; Schneider, E.; Vogt-Maranto, L.; Tuckerman, M. E., Endpoint-restricted adiabatic free energy dynamics approach for the exploration of biomolecular conforma-

- tional equilibria. J. Chem. Phys. 2018, 149, 072316. DOI: 10.1063/1.5027479
- (42) Fellah, N.; Shtukenberg, A. G.; Chan, E. J.; Vogt-Maranto, L.; Xu, W.; Li, C.; Tuckerman, M. E.; Kahr, B.; Ward, M. D. Disorderly Conduct of Benzamide IV: Crystallographic and Computational Analysis of High Entropy Polymorphs of Small Molecules. *Cryst. Growth Des.* **2020**, 20, 2670–2682.
- (43) Reiss, C. A.; Mechelen, J. B. v.; Goubitz, K.; Peschar, R. Reassessment of paracetamol orthorhombic Form III and determination of a novel low-temperature monoclinic Form III-m from powder diffraction data. *Acta Crystallogr., Sect. C: Struct. Chem.* **2018**, 74, 392–399.
- (44) Nichols, G.; Frampton, C. S. Physicochemical characterization of the orthorhombic polymorph of paracetamol crystallized from solution. *J. Pharm. Sci.* **1998**, *87*, 684–693.
- (45) Perrin, M.-A.; Neumann, M. A.; Elmaleh, H.; Zaske, L. Crystal structure determination of the elusive paracetamol Form III. *Chem. Commun.* **2009**, 3181–3183.
- (46) Liu, Y.; Gabriele, B.; Davey, R. J.; Cruz-Cabeza, A. J. Concerning Elusive Crystal Forms: The Case of Paracetamol. *J. Am. Chem. Soc.* **2020**, *142*, 6682–6689.
- (47) Wang, J.; Wolf, R. M.; Caldwell, J. W.; Kollman, P. A.; Case, D. A. Development and testing of a general amber force field. *J. Comput. Chem.* **2004**, *25*, 1157–1174.
- (48) Jakalian, A.; Bush, B. L.; Jack, D. B.; Bayly, C. I. Fast, efficient generation of high-quality atomic charges. AM1-BCC model: I. Method. *J. Comput. Chem.* **2000**, *21*, 132–146.
- (49) Li, J.; Doherty, M. F. Steady State Morphologies of Paracetamol Crystal from Different Solvents. *Cryst. Growth Des.* **2017**, *17*, 659–670.
- (50) Shtukenberg, A. G.; Tan, M.; Vogt-Maranto, L.; Chan, E. J.; Xu, W.; Yang, J.; Tuckerman, M. E.; Hu, C. T.; Kahr, B. Melt Crystallization for Paracetamol Polymorphism. *Cryst. Growth Des.* **2019**, *19*, 4070–4080.
- (51) Parks, C.; Koswara, A.; Tung, H.-H.; Nere, N.; Bordawekar, S.; Nagy, Z. K.; Ramkrishna, D. Molecular Dynamics Electric Field Crystallization Simulations of Paracetamol Produce a New Polymorph. *Cryst. Growth Des.* **2017**, *17*, 3751–3765.
- (52) Groom, C. R.; Bruno, I. J.; Lightfoot, M. P.; Ward, S. C. The Cambridge Structural Database. *Acta Crystallogr., Sect. B: Struct. Sci.* **2016**, 72, 171–179.
- (53) Chisholm, J. A.; Motherwell, S. COMPACK: a program for identifying crystal structure similarity using distances. *J. Appl. Crystallogr.* **2005**, 38, 228–231.
- (54) Macrae, C. F.; Sovago, I.; Cottrell, S. J.; Galek, P. T. A.; McCabe, P.; Pidcock, E.; Platings, M.; Shields, G. P.; Stevens, J. S.; Towler, M.; Wood, P. A. Mercury 4.0: from visualization to analysis, design and prediction. *J. Appl. Crystallogr.* **2020**, 53, 226.
- (55) van Eijck, B. P.; Kroon, J. Upack program package for crystal structure prediction: Force fields and crystal structure generation for small carbohydrate molecules. *J. Comput. Chem.* **1999**, 20, 799–812.
- (56) Tuckerman, M. E.; Yarne, D. A.; Samuelson, S. O.; Hughes, A. L.; Martyna, G. J. Exploiting multiple levels of parallelism in Molecular Dynamics based calculations via modern techniques and software paradigms on distributed memory computers. *Comput. Phys. Commun.* **2000**, *128*, 333–376.
- (57) Martyna, G. J.; Klein, M. L.; Tuckerman, M. Nosé–Hoover chains: The canonical ensemble via continuous dynamics. *J. Chem. Phys.* **1992**, *97*, 2635–2643.
- (58) Martyna, G. J.; Tuckerman, M. E.; Tobias, D. J.; Klein, M. L. Explicit reversible integrators for extended systems dynamics. *Mol. Phys.* **1996**, *87*, 1117–1157.
- (59) Martyna, G. J.; Tobias, D. J.; Klein, M. L. Constant pressure molecular dynamics algorithms. *J. Chem. Phys.* **1994**, *101*, 4177–4189.
- (60) Yu, T.-Q.; Alejandre, J.; López-Rendón, R.; Martyna, G. J.; Tuckerman, M. E. Measure-preserving integrators for molecular dynamics in the isothermal—isobaric ensemble derived from the Liouville operator. *Chem. Phys.* **2010**, *370*, 294–305.

- (61) Rosso, L.; Tuckerman, M. E. An Adiabatic Molecular Dynamics Method for the Calculation of Free Energy Profiles. *Mol. Simul.* **2002**, 28, 91–112.
- (62) Liu, Y.; Tuckerman, M. E. Generalized Gaussian moment thermostatting: A new continuous dynamical approach to the canonical ensemble. *J. Chem. Phys.* **2000**, *112*, 1685–1700.
- (63) Lippert, G.; Hutter, J.; Parrinello, M. A hybrid Gaussian and plane wave density functional scheme. *Mol. Phys.* **1997**, 92, 477–487.
- (64) Hutter, J.; Iannuzzi, M.; Schiffmann, F.; VandeVondele, J. cp2k: atomistic simulations of condensed matter systems. *Wiley Interdiscip. Rev.: Comput. Mol. Sci.* **2014**, *4*, 15–25.
- (65) VandeVondele, J.; Krack, M.; Mohamed, F.; Parrinello, M.; Chassaing, T.; Hutter, J. QUICKSTEP: Fast and accurate density functional calculations using a mixed Gaussian and plane waves approach. *Comput. Phys. Commun.* **2005**, *167*, 103–128.
- (66) Perdew, J. P.; Burke, K.; Ernzerhof, M. Generalized Gradient Approximation Made Simple. *Phys. Rev. Lett.* **1996**, 77, 3865–3868.
- (67) Grimme, S.; Antony, J.; Ehrlich, S.; Krieg, H. A consistent and accurate ab initio parametrization of density functional dispersion correction (DFT-D) for the 94 elements H-Pu. *J. Chem. Phys.* **2010**, 132, 154104.
- (68) Goedecker, S.; Teter, M.; Hutter, J. Separable dual-space Gaussian pseudopotentials. *Phys. Rev. B: Condens. Matter Mater. Phys.* 1996, 54, 1703–1710.
- (69) Krack, M. Pseudopotentials for H to Kr optimized for gradient-corrected exchange-correlation functionals. *Theor. Chem. Acc.* **2005**, 114, 145–152.